Pressure-induced antiferromagnetic dome in the heavy-fermion Yb$_2$Pd$_2$In$_{1-x}$Sn$_x$ system

G. Lamura,[1,*] I. J. Onuorah,[2] P. Bonfà ,[2,3] S. Sanna,[4] Z. Shermadini,[5] R. Khasanov,[5] J.-C. Orain,[5] C. Baines,[5]
F. Gastaldo,[6] M. Giovannini,[6] I. Čurlík,[7] A. Dzubinska,[8] G. Pristas ,[9] M. Reiffers,[7,9] A. Martinelli ,[1] C. Ritter,[10]
B. Joseph ,[11] E. Bauer,[12] R. De Renzi ,[2] and T. Shiroka [5,13]

[1]*CNR-SPIN, I-16152 Genova, Italy*
[2]*Department of Mathematical, Physical and Computer Sciences, University of Parma, 43124 Parma, Italy*
[3]*Centro S3, CNR-Istituto Nanoscienze, 41125 Modena, Italy*
[4]*Department of Physics and Astronomy, University of Bologna, 40127 Bologna, Italy*
[5]*Laboratory for Muon Spin Spectroscopy, Paul Scherrer Institut (PSI), CH-5232 Villigen, Switzerland*
[6]*Dipartimento di Chimica e Chimica Industriale, University of Genova, 16146 Genova, Italy*
[7]*Faculty of Humanities and Natural Sciences, University of Prešov, SK 081 16 Prešov, Slovakia*
[8]*CPM-TIP, University Pavol Jozef Safarik, 041 54 Kosice, Slovakia*
[9]*Institute of Experimental Physics of the Slovak Academy of Sciences (IEP SAS), 040 01 Košice, Slovakia*
[10]*Institut Laue-Langevin, 38042 Grenoble, France*
[11]*GdR IISc-ICTP, Elettra-Sincrotrone, Basovizza, 34149 Trieste, Italy*
[12]*Institute of Solid State Physics, TU Wien, A-1040 Wien, Austria*
[13]*Laboratorium für Festkörperphysik, ETH-Hönggerberg, CH-8093 Zürich, Switzerland*

In the heavy-fermion system Yb$_2$Pd$_2$In$_{1-x}$Sn$_x$, the interplay of crystal-field splitting, Kondo effect, and Ruderman-Kittel-Kasuya-Yosida interactions leads to complex chemical-, pressure-, and magnetic-field phase diagrams still to be explored in full detail. By using a series of techniques, we show that even modest changes of parameters other than temperature are sufficient to induce multiple quantum-critical transitions in this highly susceptible heavy-fermion family. In particular, we show that, above ∼10 kbar, hydrostatic pressure not only induces an antiferromagnetic phase at low temperature, but it likely leads to a reorientation of the Yb magnetic moments and/or the competition among different antiferromagnetic configurations.

I. INTRODUCTION

Ytterbium-based intermetallic compounds represent one of the most interesting classes of materials for investigating the interplay of crystal-field splitting, Kondo effect, and Ruderman-Kittel-Kasuya-Yosida (RKKY) interactions. Given their comparable energy scales, it is not surprising that the resulting ground state can easily be tuned via external pressure, chemical substitution, or applied magnetic fields [1,2]. Within the larger class of heavy-fermion (HF) compounds, Yb-based materials are among the best examples of quantum critical systems showing a non-Fermi liquid behavior. This is due to the manifest sensitivity of the Yb^{2+} electronic configuration to chemical and external pressure. Thus, an increase in pressure "squeezes" one of the Yb $4f$ electrons out of its shell, driving the nonmagnetic Yb^{2+} ($4f^{14}$, $J = 0$) to magnetic Yb^{3+} ($4f^{13}$, $J = 7/2$, $\mu = 4.52$ μ_B). As a consequence, the Kondo effect is weakened, while the RKKY-mediated exchange interactions among the Yb ions are enhanced, a favorable condition for the onset of a long-range magnetically ordered phase [3–7]. This is precisely the case of Yb$_2$Pd$_2$In$_{1-x}$Sn$_x$, previously investigated via macroscopic techniques and lately studied also via μSR, at both ambient- and high-pressure

conditions, in the stoichiometric $x = 1$ case [6]. While, in general, there is consensus with regard to the broad picture, key details are still missing. In particular, the joint effects of chemical- and applied pressure, as well as the resulting phase diagrams and the type of magnetic order remain largely unexplored to date.

Here, by combining a range of experimental techniques, including magnetic susceptibility, muon-spin rotation (μSR), x-ray, and neutron diffraction, we map out the temperature-, pressure-, and composition phase diagram of this prototypical HF system. In particular, we show that externally applied pressure reinforces the effects of chemical pressure (here achieved via In/Sn substitution) by extending the magnetically ordered dome and by reordering the Yb magnetic moments into a new antiferromagnetic phase, whose critical temperature reaches $T_N \sim 4.9$ K at 23.4 kbar at the optimum doping. Numerical calculations and symmetry considerations proved essential in clarifying the new magnetic structure adopted at high pressure.

II. CRYSTAL STRUCTURE, X-RAY DIFFRACTION AND DC MAGNETIZATION

A series of Yb$_2$Pd$_2$In$_{1-x}$Sn$_x$ polycrystalline samples with nominal compositions $x = 0, 0.3, 0.6, 0.8$ were prepared from
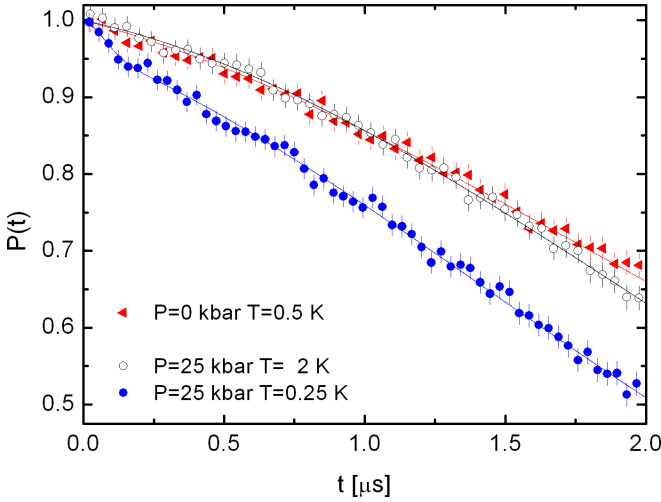
*Corresponding author: gianrico.lamura@spin.cnr.it

FIG. 1. Time-domain ZF-μSR polarization for the $x = 0$ case measured at $T = 0.5$ K for $p = 0$ kbar (◄) and at $T = 2$ K (○) and 0.25 K (●) for $p = 25$ kbar. Only in the last case a tiny depolarization is seen at short times ($t < 0.2$ μs).

stoichiometric amounts of pure elements by high-frequency melting of the constituent materials in a closed tantalum crucible. A subsequent 1-week heat treatment at 1250 K was used to ensure chemical homogeneity. All the compounds of this series crystallize in the tetragonal $P4/mbm$ space group, where Yb occupies the $4h$ sites. Systematic x-ray diffraction and dc magnetization measurements performed on all the samples confirmed the absence of spurious phases (within the sensitivity of the respective techniques [8]). Samples were further investigated via high-pressure synchrotron x-ray diffraction at the Elettra source and neutron powder diffraction at the Institute Laue-Langevin (ILL). The detailed results of the above measurements are reported in the Appendices A–C and in Ref. [9].

III. μSR MEASUREMENTS

The muon-spin relaxation measurements under hydrostatic-pressure conditions in the 0- to 25-kbar range, from 0.25 to 10 K, were carried out at the General Purpose Decay-Channel (GPD) spectrometer of the SμS muon source of the Paul Scherrer Institut (Villigen, Switzerland). The external pressure was applied by using a double-wall piston-cylinder pressure cell made of MP35N alloy. Daphne oil 7373 was used as a pressure-transmitting medium to achieve nearly hydrostatic conditions across the whole pressure range [10,11]. To determine the exact pressure at low temperature, a small piece of indium was placed next to the sample. The pressure-dependent shift of its superconducting transition $T_c(p)$ was determined via ac susceptometry [10,11]. Due to the small mass of In, its contribution to the μSR background is negligible.

Figures 1 and 2 show the time-dependent, zero-field (ZF) muon-spin depolarization at short time for all the samples under test at representative temperatures and applied pressures. As a general feature, highly damped coherent oscillations are seen to develop on increasing the Sn content or the applied pressure, thus providing key evidence about the onset of a long-range magnetic order with a large degree of inhomogeneity. To determine the parameters of these coherent precessions and to disentangle the spurious contribution of the pressure cell to the total signal, the time-dependent muon-spin depolarization was fitted by using the model:

$$P(t) = \frac{A^{\mathrm{ZF}}(t)}{A_{\mathrm{tot}}^{\mathrm{ZF}}(0)} = a_{\mathrm{bg}}\, g(t) + (1 - a_{\mathrm{bg}})$$
$$\times \sum_{i=1}^{N} w_i [a_{T_i} f_i(\gamma_\mu B_\mu t) D_{T_i}(t) + a_{L_i} D_{L_i}(t)]. \quad (1)$$

Here $A_{\mathrm{tot}}^{\mathrm{ZF}}(0)$ is the high-temperature value of the initial asymmetry, whereas a_{bg} accounts for the fraction of incoming
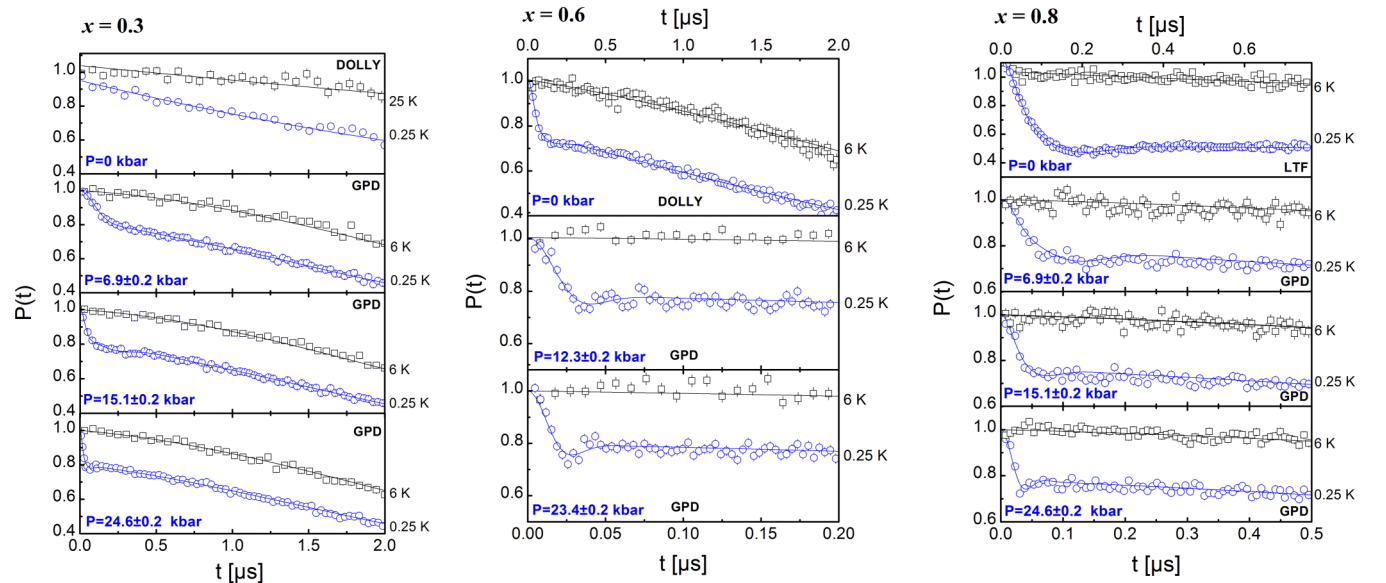

FIG. 2. Time-domain ZF-μSR polarization measured at base temperature (0.25 K) and above T_N (typically at 6 K) at ambient- and under applied-pressure conditions for the $x > 0$ case. From left to right, the Sn concentrations are $x = 0.3$, 0.6, and 0.8. The appearance of oscillations under applied pressure indicates the onset of a pressure-induced antiferromagnetic phase.

muons stopped outside the sample. Regarding this last parameter, three cases can be distinguished: (i) a_{bg} is almost zero during the reference experiments performed at the low-background spectrometer Dolly (samples with $x = 0.3$ and 0.6) and (ii) a_{bg} coincides with the muon fraction implanted in the Ag sample holder during experiments on $x = 0.8$ sample at Low Temperature Facility (LTF) at the SμS, PSI. In this case we assume $g(t) = e^{-\lambda_{Ag}t}$, with both a_{bg} and λ_{Ag} being determined at the lowest temperature and kept fixed during subsequent fits [12]. (iii) During the GPD measurements, a_{bg} accounts for the fraction of muons implanted in the pressure cell [13]. In this case, $g(t)$ corresponds to a Gaussian Kubo-Toyabe function multiplied by an exponential damping [10,14].

The coherent muon precession in the magnetically ordered phase is described by the $f(t)$ function, while the $D_{T_i}(t)$ and $D_{L_i}(t)$ terms account for a possible damping. Here $D_{T_i}(t)$ reflects the static distribution of local magnetic fields, whereas $D_{L_i}(t)$ describes the dynamical relaxation processes. B_μ^i is the magnetic field at the ith muon implantation site and $\gamma_\mu = 2\pi \times 135.53$ MHz/T is the muon gyromagnetic ratio; a_{T_i} and a_{L_i} refer to muons probing local magnetic fields in the transverse (T) or longitudinal (L) direction with respect to the initial muon-spin polarization. The sum over i generalizes Eq. (1) to the case of diverse inequivalent crystallographic implantation sites, whose population weights w_i satisfy the normalization condition $\sum_i^N w_i = 1$. In the following, we specify the above parameters in the context of each case.

A. $x = 0$

Figure 1 shows the short-time ZF μSR depolarization for the pure In case. The polarization $P(t)$ can be fitted by a single Gaussian decay at both standard- and applied-pressure conditions, provided the temperature is not very low. This type of decay is normally associated with randomly oriented nuclear dipolar fields. However, when (at 25 kbar) the temperature is lowered to 0.25 K, a small transverse component appears, indicating that ∼15% of the sample develops weak magnetic correlations. Such behavior suggests that Yb_2Pd_2In is on the verge of quantum criticality, with a magnetic phase transition presumably occurring at higher pressure.

B. $x = 0.3$

The low-background ambient-pressure data taken at $T = 25$ K [Fig. 2(a), top panel] are well fitted by a single Gaussian depolarization, reflecting the randomly oriented nuclear dipolar fields. At the lowest temperature a small depolarization appears, suggesting that also in this case, at ambient pressure the system is likely at the verge of a magnetic instability. Interestingly, by progressively increasing the pressure (to 12.3 and 23.4 kbar) a strongly damped oscillation appears at 0.25 K. In this case, the fitting function describing the sample contribution consists of two transverse components, one of which is a damped Gaussian cosine [15] and the other is represented by a Gaussian decay. The corresponding longitudinal components can be merged into a single Lorentzian decay. It is worth noting that the frequency of the oscillating part increases rapidly with increasing pressure, suggesting the proximity to a pressure-induced magnetic order.

C. $x = 0.6$

As shown in Fig. 2 (top panel), the low background data taken at ambient pressure and $T = 0.25$ K are well fitted by one transverse component, consisting of a damped Gaussian cosine [15] and a single Lorentzian decay. This differs from the $x = 0.3$ case where, at ambient pressure, a weakly decaying Gaussian function is sufficient to describe the data. The previous two-component fitting function was successfully adopted also for the measurements under pressure [Fig. 2(b), lower panels]. Here, too, a sudden increase of muon-precession frequency with increasing pressure occurs.

D. $x = 0.8$

At ambient pressure, the low background data taken at $T = 6$ K, i.e., above T_N [Fig. 2, top panel], are well fitted by a single Gaussian depolarization, reflecting the randomly oriented nuclear dipolar moments. At the lowest temperature, the damped oscillation could be fitted by two transverse components, of which one is a damped Gaussian cosine term [15] and the other is a Gaussian decay. The two longitudinal signals, again merged into one, are fitted by a single Lorentzian exponential. On applying pressure, the same fitting function was adopted [Fig. 2, lower panels]. Also in this case, the frequency of the oscillating component increases rapidly with increasing pressure.

Figures 3(a)–3(c) show the evolution of the oscillating component of the local field B_μ as a function of temperature for all the applied pressures. Generally, in all cases, we note a steep increase of the internal magnetic field. In particular, for $x = 0.6$, the internal field shows a fivefold enhancement from its ambient-pressure value.

Figure 4 summarizes the evolution of the local-field widths for both transverse components at the lowest temperature as a function of applied pressure. We note a remarkable broadening of both widths at the muon implantation sites on increasing pressure.

The magnetic volume fraction V_M in the ordered phase was determined in two different ways. In case of ambient pressure experiments, it was extracted from the total longitudinal component by means of $V_M(T) = 3(1 - a_\parallel^{tot})/2$ [16,17]. In case of applied pressure, the magnetic volume fraction was estimated from the temperature evolution of the oscillating paramagnetic fraction in a weak transverse field (wTF) μSR experiment ($\mu_0 H = 3$ mT). The evolution of the magnetic volume fraction with the applied pressure is shown in Figs. 3(d)–3(f) for all those cases where a magnetically ordered phase could be detected.

We note two important features: (i) the transition widths remain rather narrow, never exceeding 1 K, irrespective of the applied pressure and (ii) the magnetic ordering temperature increases steeply with applied pressure. For instance, in the optimally substituted $x = 0.6$ sample, T_N at 23 kbar reaches twice its ambient-pressure value. In the explored pressure range T_N increases almost linearly with pressure. The differential increment (slope) is maximal for $x = 0.3$ (ca. 0.15 K/kbar), then it gradually decreases, to saturate at 0.07 K/kbar at higher tin content. Such values are remarkably high for a heavy-fermion compound (compared, for instance, with 0.016 K/kbar for $CeNiSiH_x$ [18]).
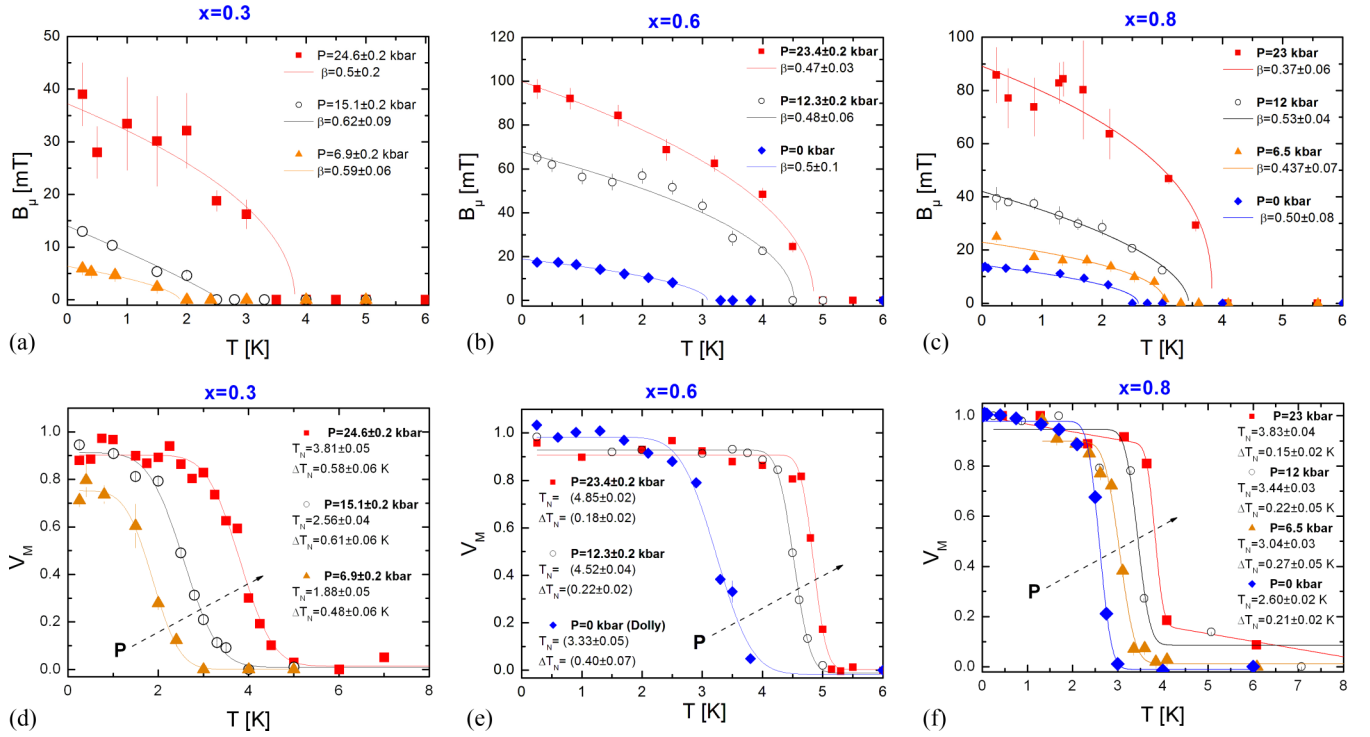
FIG. 3. Internal magnetic fields B_μ (top panels) and magnetic volume fractions (bottom panels), as determined from fits of the ZF- and wTF μSR data collected at different applied pressures for the $x = 0.3$, 0.6, and 0.8 cases. The continuous lines in the top panels represent numerical fits according to a Landau mean field theory $B = B_0(1 - T/T_N)^\beta$ with β as free parameter ($\beta = 1/2$ in the case of 2nd order transitions). In the bottom panels, the continuous lines represent numerical fits to an *erf* model function (see text for details).

The datasets shown in Fig. 3 allow us to build the full p-T-x and p-B_μ-x phase diagrams, as shown in Fig. 5. Some interesting features can be highlighted: (i) For $x = 0$, at $T = 0.25$ K and $p = 25$ kbar the system is already on the verge of quantum criticality, as almost 15% of the sample develops weak magnetic correlations, suggesting that a possible phase

FIG. 4. Internal magnetic-field widths for the two transverse components, $\Delta B_\mu^{\rm osc}$ (top panel) and $\Delta B_\mu^{\rm exp}$ (bottom panel), measured at the lowest temperature for the samples with $x = 0.3$, 0.6, and 0.8. The field width for the nonoscillating Gaussian decay could not be detected for $x = 0.6$ (see text for details).

transition might occur at higher pressures. (ii) For $x = 0.3$, at $T = 0.25$ K and ambient pressure the system is again at the verge of a magnetic instability, with only a small volume fraction developing magnetic correlations. On increasing pressure, a long-range magnetic order appears, with transition temperatures and local magnetic fields reaching 3.8 K and 40 mT, respectively, at 24.6 kbar. (iii) In the $x = 0.6$ (optimally doped) and $x = 0.8$ cases a long-range magnetic order is already present at ambient pressure and $T = 0.25$ K. At the highest applied pressure the magnetic ordering temperature almost doubles and the internal field shows a fivefold increase from its ambient-pressure value. (iv) On increasing pressure, we observe a remarkable broadening of the field width at each muon implantation site. (v) For $x = 1.0$, previous experiments have shown that a magnetically ordered phase appears only for pressures above 10 kbar [6].

In summarizing this section we conclude that (a) below T_N, all the tested compounds order magnetically over the whole sample volume; (b) the magnetic transition widths remain narrow even at the highest applied pressures, while T_N increases steeply with pressure; and (c) the internal field increases steeply above a critical pressure $p_{\rm cr} \sim 10$ kbar. This is accompanied by a progressive broadening of the field widths.

IV. DFT AND DIPOLAR FIELD CALCULATIONS

Density functional theory– (DFT) based calculations have proven highly successful in locating the muon implantation sites in several materials [19–23]. Based on this, we performed structural relaxations by DFT to determine the muon
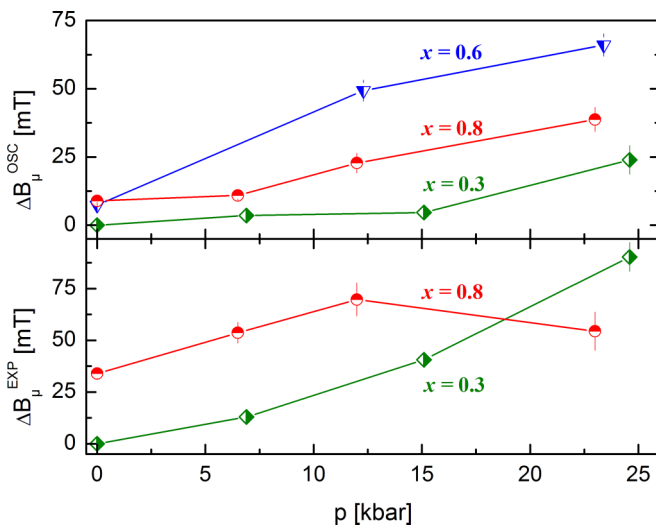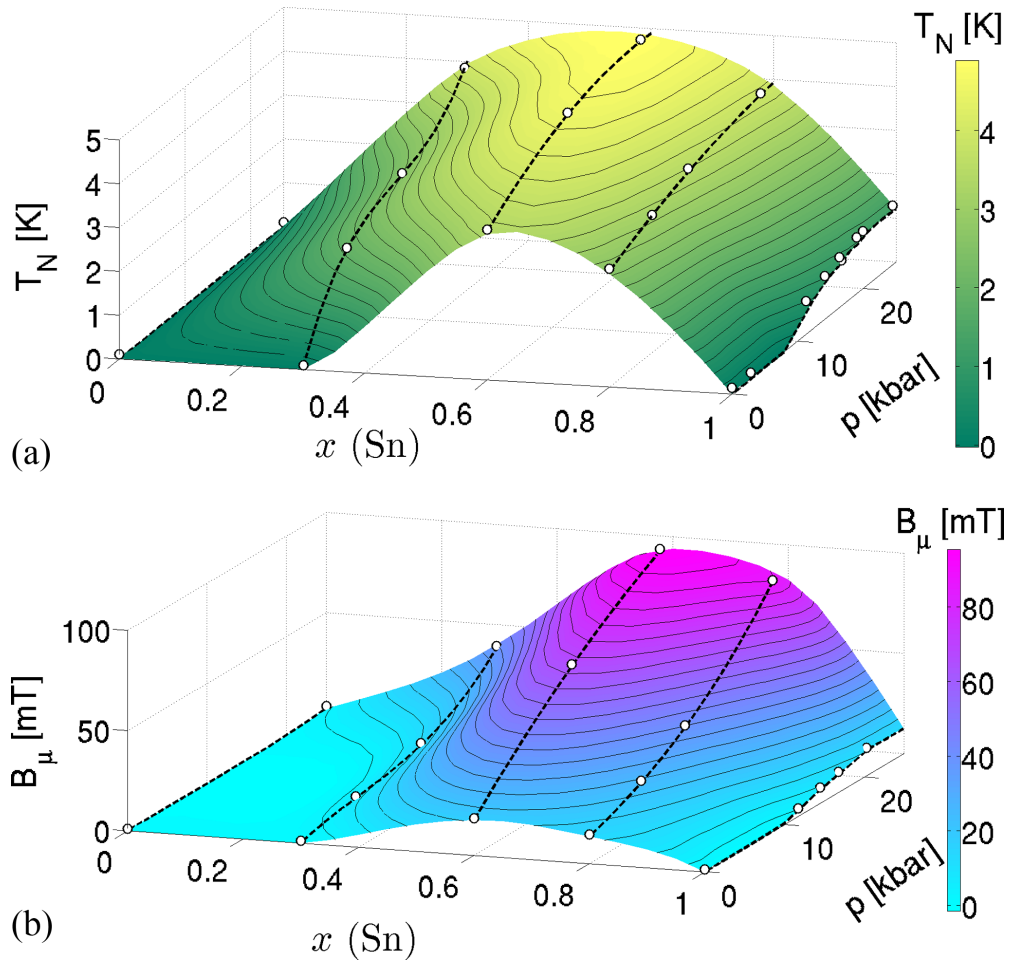
FIG. 5. *p-T-x* (a) and *p-B-x* (b) phase diagrams of the $Yb_2Pd_2In_{1-x}Sn_x$ system. White dots represent experimental points, while three-dimensional surfaces and dashed lines are interpolations obtained via polynomial fits. Note the increased B_μ field at high pressure.

stopping sites and, thus, get a better understanding of the evolution of B_μ with applied pressure and as a function of In/Sn substitution. Here we consider the representative cases of $x = 1.0$ and $x = 0.5$.

To determine the muon implantation sites we used (0.45, 0.45, 0.54) as a starting position, since it corresponds to the minimum of the electrostatic potential in Yb_2Pd_2Sn (see Appendices D and E). The final muon site resulting from structural relaxations (0.459, 0.484, 0.50) is close to that obtained from the electrostatic potential minima but has a higher site symmetry ($8j$ instead of $16l$). Notably, we find four symmetry-equivalent sites that are only 0.6 Å apart from each other. At first approximation, we therefore assume the muon to occupy a delocalized region, spread over these equivalent closely spaced sites. This implies the need to consider muon delocalization in the subsequent local dipolar-field calculations in the following form: $\langle B \rangle = \langle \phi_\mu | B | \phi_\mu \rangle \approx \frac{1}{4} \sum_{i=1}^{4} B_i$. This procedure yields similar results to those where the muon is located at the centroid (0.5, 0.5, 0.5) position (of the four equivalent sites). To simplify the description, we report the results for this second case.

It is worth noting that, despite the presence of two transverse-field components in the $x = 0.3$ and 0.8 samples (suggesting two nonequivalent muon sites), DFT calculations predict only one muon implantation site. Such apparent

inconsistency could be resolved by considering the *disorder* induced by either the In/Sn substitution or by applied pressure. Thus, at low temperatures, the whole sample could be pictured as an ensemble of nanometric size domains with either long- or short-range magnetic order. Such effect becomes increasingly relevant with increasing pressure, as suggested by the considerable rise in the local field width (see Fig. 4). Magnetic frustration, expected to increase with increasing pressure, may further reinforce such effects. In this context, in the limit of even higher pressures, $Yb_2Pd_2In_{1-x}Sn_x$ could be at the verge of a transition toward a nonmagnetic phase of a "valence bond solid" (VBS), as already proposed in Ref. [24] to explain the vanishing of the AF phase above 40 kbar in the $x = 1.0$ case [6].

We evaluate the dipolar field at the muon site (due to Yb magnetic moments) by making the following assumptions: (i) B_μ is predominantly of dipolar origin and (ii) the applied hydrostatic pressure, when lower than p_{cr} (see Appendix A), distorts negligibly the atomic surrounding in the crystallographic unit cell. Thus, neither the muon implantation site(s) nor the propagation vector change significantly with pressure. (iii) The ordered Yb magnetic moment is set to 1 μ_B, independently of the tin content and the applied pressure. This strong assumption is reasonably verified at ambient pressure, where the Yb magnetic moment does not vary by more than

TABLE I. The 10 magnetic structures calculated by MAXMAGN code (labeled I to X) for the parent space group $P4/mbm$, that allow a nonzero magnetic moment on Yb, with propagation vector $(0,0,0.5)$ [5,9]. We report also the magnetic structure on the four symmetry-equivalent magnetic Yb ions in half of the unit cell doubled along the c axis and the calculated muon dipolar field B_{dip} in units of mT.[a]

Label	Magnetic group	Magnetic structure[b]				B_{dip} (mT) (s.d.)
		Yb1	Yb2	Yb3	Yb4	
I	P_c4_2/mnm	$(m_x, -m_x, 0)$	$(-m_x, m_x, 0)$	$(-m_x, -m_x, 0)$	$(m_x, m_x, 0)$	6.18 (1.91)
II	P_c4_2/mbc	$(m_x, m_x, 0)$	$(-m_x, -m_x, 0)$	$(m_x, -m_x, 0)$	$(-m_x, m_x, 0)$	3.79 (1.66)
III	P_c4_2/mbc	$(0, 0, m_z)$	$(0, 0, m_z)$	$(0, 0, -m_z)$	$(0, 0, -m_z)$	3.58 (1.76)
IV	P_c4/mnc	$(0, 0, m_z)$	$(0, 0, m_z)$	$(0, 0, m_z)$	$(0, 0, m_z)$	245.22 (4.95)
V	P_c4/mnc	$(m_x, m_x, 0)$	$(-m_x, -m_x, 0)$	$(-m_x, m_x, 0)$	$(m_x, -m_x, 0)$	4.66 (1.68)
VI	P_c4/mbm	$(m_x, -m_x, 0)$	$(-m_x, m_x, 0)$	$(m_x, m_x, 0)$	$(-m_x, -m_x, 0)$	6.87 (1.89)
VII	C_cmcm	$(0, 0, 0)$	$(0, 0, 0)$	$(0, 0, m_z)$	$(0, 0, -m_z)$	2.25 (1.21)
VIII[c]	C_cmcm	$(m_x, m_x, 0)$	$(m_x, m_x, 0)$	$(m_y, m_y, 0)$	$(m_y, m_y, 0)$	122.61 (4.53)
IX	P_bnma	$(0, 0, m_z)$	$(0, 0, -m_z)$	$(0, 0, -m_z)$	$(0, 0, m_z)$	3.03 (1.25)
X[c]	P_bnma	$(m_x, m_y, 0)$	$(m_x, m_y, 0)$	$(-m_x, m_y, 0)$	$(-m_x, m_y, 0)$	100.17 (4.54)

[a]Yb1, Yb2, Yb3, Yb4 at $(0.1724, 0.6724, c/2)$, $(0.8276, 0.3276, c/2)$, $(0.3276, 0.1724, c/2)$, $(0.6724, 0.8276, c/2)$; $c = 0.5$.
[b]Dipolar field at the muon position $(0.5, 0.5, 0.5)$ for $x = 0.5$. The In/Sn substitution-induced displacements on the Yb ions were considered. The values in parenthesis labeled (s.d.) represent the standard deviation considering different random displacements.
[c]In these cases $m_x = m_y$ was considered.

40% (as deduced from neutron scattering measurements [5] at different In/Sn substitutions). Very recent neutron powder diffraction measurements as a function of pressure (to 14 kbar) on an $x = 0.6$ sample also show only an increase of 11% of the ordered magnetic moment (Appendix C). Since the dipolar field contribution at the muon implantation site is linear with the ordered magnetic moment, the above tiny variations cannot justify the 10-fold increase of B_μ reported in Fig. 3. Therefore, we can reasonably assume that the Yb magnetic moment is almost constant, at least up to p_{cr}.

Given the propagation vector $k = (0, 0, \frac{1}{2})$ [5,9], the MAXMAGN code on the Bilbao crystallographic server [25,26] identifies 10 maximal magnetic space groups for the parent space group $P4/mbm$ (No. 127), allowing a nonzero field on Yb. These are labeled I to X and reported in Table I together with the corresponding magnetic structures on the Yb atoms.

For all these magnetic structures the dipole sum was calculated using a $100 \times 100 \times 100$ supercell. In a perfect stoichiometric crystal, all the structures except IV, VIII, and X have zero dipolar fields by symmetry. However, Sn/In substitutions induce small in-plane displacements of the Yb atoms and of the muon position. The extent of these displacements was reproduced through several random realizations of the $x = 0.5$ concentration. The small dipolar field that arises as a consequence of the Yb displacements was evaluated by averaging on a set of 32 interstitial positions. This leads to local fields ranging from 3 to 10 mT in those structures where the field would otherwise have been zero by symmetry. The full set of results for the 10 magnetic structures, obtained after averaging on the $x = 0.5$ lattice realizations, is summarized in Table I. The additional averaging over the four equivalent muon sites has a negligible effect. Yet, for completeness, we report it in Appendix E.

Notably, the calculated dipolar field for the magnetic structure suggested by neutron scattering at ambient pressure [structure VI, observed for $x(\text{Sn}) = 0.5\text{–}0.9$] [5,9] is found to be about 7 mT. This field value agrees well with those

sensed by muons in the Sn/In substituted samples at ambient pressure, hence justifying our original omission of the contact-field contribution. At the same time, the above result suggests that the Yb magnetic moments cannot remain in the magnetic structure VI also at high pressures, where the measured internal field is 4 to 10 times the expected one. For the same reason, none of the magnetic structures I–III, V, VII, and IX can describe the Yb ordering observed at high pressure for $x = 0.3$, 0.6, and 0.8, since in all these cases the calculated dipolar fields range from 3 to 7 mT.

Of the 10 long-range orders considered here, only three justify the drastic increase of local field at the muon site for $p > p_{\text{cr}}$. These include the magnetic structures IV, VIII, and X, marked in bold in Table I and shown in Fig. 6. However, since also a contact hyperfine component may be present, we refrain from making direct comparisons between the measured and calculated local field.

To summarize, our results strongly suggests a *reordering of the Yb magnetic moments* at high pressures, above p_{cr}. The above-mentioned recent low-temperature neutron and room temperature synchrotron diffraction data (see Ref. [9] and Appendices A and C), both collected under applied pressure, suggest *no changes in the magnetic and crystalline structure up to p_{cr}*. However, above p_{cr} a structural transition does take place. Consequently, we considered also the supposed high-pressure monoclinic structure $P2_1/c$ (Appendix D). In this case, four irreducible representations allow for a nonzero magnetic moment on the Yb ion. If the Yb moments are constrained to lie either along a or in the bc plane, with $|m_b| = |m_c|$, then the local field at the muon site does not change appreciably with respect to the values identified for the tetragonal low-pressure structure. This implies that the structural transition at p_{cr} does not appreciably change the calculations of the internal field B_μ done for the 10 models deduced for the tetragonal symmetry summarized in Table I.

At the same time neutron powder diffraction in the $x = 0.6$ case revealed a stable magnetic structure up to 14 kbar, suggesting that a pressure-induced magnetic phase transition—if
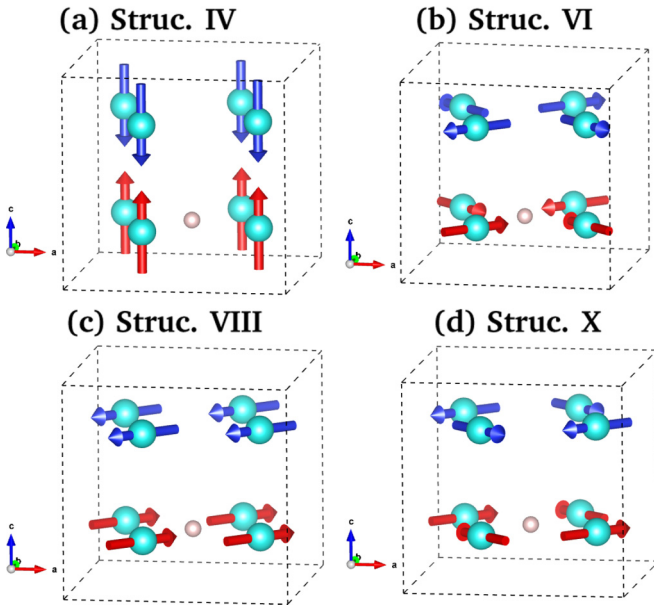
FIG. 6. Magnetic structures IV (a), VI (b), VIII (c), and X (d) listed in Table I for a doubled unit cell along c. Structure VI is the known AF structure at ambient pressure, while structures IV, VIII, and X justify the local field B_μ we measure at high pressure. For clarity only the Yb atoms and the muon (pink sphere) are shown. The structures were drawn using VESTA [27].

any—could take place only at very high pressures beyond the instrument limits. At intermediate pressure values, we expect the effects of the different competing AF-ordered phases to correspond to the magnetic structures IV, VIII, and X mentioned above. These competing orders could result in magnetic frustration and, hence, significantly enhance the local field width at high pressure. At the same time, all these magnetic structures are compatible with the large increase of magnetic field observed above p_{cr} [see Fig. 5(b)].

V. DISCUSSION

The ground-state electronic properties of heavy-fermion compounds are determined by a subtle interplay between the RKKY and Kondo interactions, whose characteristic temperature (energy) scales are $T_{RKKY} \propto g^2$ and $T_K \propto e^{-1/g}$, with $g = \Gamma/\pi\Delta_f$, a coupling parameter. Here $\Gamma \propto V_{fc}^2$, where V_{fc} represents the overlap between the wave functions of $4f$ and conduction electrons, while Δ_f is the excitation energy between the magnetic and nonmagnetic electronic configurations [6]. In most Yb systems, valence fluctuations and the reduced size of $4f$ Yb ions rule out significant changes of V_{fc} up to 25 kbar [6]. Consequently, in the considered pressure range, the coupling strength g is determined almost entirely by the excitation energy Δ_f.

At the boundaries of the p-T-x phase diagram, i.e., at low hydrostatic pressures in the pure In or Sn case (i.e., for $x \sim 0$ or 1), the excitation energy Δ_f is expected to assume its minimum value, which maximizes g [6]. In turn, this is reflected in T_K values up to 20–30 K, resulting in a nonmagnetic ground state with non-Fermi-liquid properties, as confirmed by our μSR measurements (see Fig. 5). In this case, our Yb-based

Kondo-lattice system is found in the Kondo screening region of the Doniach phase diagram [28].

The application of hydrostatic or chemical pressure implies a reduction of the unit cell volume [4]. Moderate hydrostatic pressure has negligible effects on the Yb^{3+} valence, as confirmed by x-ray absorption spectroscopy in the partial fluorescence yield mode and by resonant x-ray emission spectroscopy under applied pressure [7]. Also the In/Sn substitution, (chemical pressure), does not distinctly affect valence, since dc susceptibility measurements indicate almost constant Yb magnetic moments in the paramagnetic state, independent of tin concentration (Appendix B). In this region of the phase diagram, an increase of pressure induces a growth of resistivity [3,4], corresponding to a reduced f-c electron coupling and to an increased excitation energy Δ_f. Both of them stabilize the antiferromagnetic phase [6], clearly suggesting that pressure (either hydrostatic or chemical) shifts a Kondo-lattice system toward the RKKY interaction regime in the Doniach phase diagram [28].

As shown in Fig. 5(a), the antiferromagnetic phase covers a wide area of the p-T-x phase diagram. At ambient pressure it spans only the $0.3 < x < 0.9$ range. However, on increasing pressure, the AF region extends to cover the full $0 < x < 1$ range, albeit with a slightly asymmetric distribution of T_N temperatures. Thus, for $x = 0$, the system is at the verge of a magnetic transition at a pressure of 25 kbar, while for $x = 1$ the AF phase has its onset at only about 10 kbar. The fine balance between chemical pressure and effective doping, here realized through the In/Sn substitution, may explain the slightly off-centered dome shape in the p-T-x phase diagram. In addition, Mössbauer studies evidence different types of ground states in the pure In and Sn systems [6,29]. Off-centered features might thus result naturally.

Similar features are also found in the p-B_μ-x phase diagram, shown in Fig. 5(b). Interestingly, for $x < 1$, a marked change in the slope of the B_μ vs. p plot is clearly visible at about p_{cr} (see continuous lines). Such pressure value coincides with that where a structural phase transition was shown to occur at ambient temperature (see Fig. 7) for any x(Sn) value, except for $x = 1$. In this case no structural transitions could be detected (up to 100 kbar). In this case, we note also that the internal field B_μ never exceeds the values found at ambient pressure in the AF dome [30]. Consequently, the significant increase of local magnetic field observed in the central part of the p-B_μ-x phase diagram cannot be ascribed to a distinct change of the Yb magnetic moment, the latter being ruled out by our dipolar-field calculations. We suggest, instead, that the steep increase in the local magnetic field is due to a *reorientation* of the Yb magnetic substructure and/or to magnetic frustration resulting from the *competition of at least three different AF magnetic structures*. Since such reordering occurs at $p > p_{cr}$, it is very tempting to assume that the change in magnetic structure is most likely driven by the above mentioned structural transition.

Finally, we address the significant increase in T_N with increasing pressure. To this aim it is instructive to compare the quantum critical behavior of Ce- with Yb-based systems [31,32]. Both Ce and Yb exhibit a trivalent magnetic state (Ce^{3+}, $4f^1$ vs. Yb^{3+}, $4f^{13}$), which can fluctuate to a nonmagnetic state, corresponding to an empty $4f^0$ shell for

Ce and to a filled ($4f^{14}$) shell for Yb. To a first approximation, in both cases pressure leads to a delocalization of the $4f$ electrons. However, while this drives Ce toward a nonmagnetic $4f^0$ state, in Yb it favors the magnetic $4f^{13}$ state, in an almost specular behavior, known as the mirrorlike behavior of cerium and ytterbium. This implies a reinforced magnetic order in Yb-based systems under applied pressure, as indeed observed, e.g., in YbCu$_2$Si$_2$ [33] or in YbRh$_2$Si$_2$ [34], and to its suppression in Ce-based systems as, e.g., in CeRh$_2$Si$_2$ [34] (where an initial T_N of 35 K goes to zero in only 12 kbar).

VI. CONCLUSIONS

The intriguing magnetic behavior of Yb$_2$Pd$_2$In$_{1-x}$Sn$_x$ was studied mostly via μSR spectroscopy and elucidated by detailed DFT calculations. Both hydrostatic and chemical pressure (the latter through In/Sn substitution) promote an AF coupling of Yb^{3+} magnetic moments. The internal field evolution with pressure suggest a possible reorientation of the Yb moments and/or the presence of frustrated magnetism, most likely due to different competing AF interactions above p_{cr} and is presumably driven by a structural phase transition.

Neutron Diffraction data are available from ILL [37].

ACKNOWLEDGMENTS

APPENDIX A: X-RAY DIFFRACTION

The synchrotron x-ray powder diffraction (XRPD) measurements were carried out at 300 K at the Xpress beamline of Elettra (Trieste, Italy). Two datasets were collected: at ambient pressure using a radiation wavelength $\lambda = 0.700$ Å (for $x = 0.0, 0.3, 0.4, 0.6, 0.8$), and as a function of pressure—up to ∼35 kbar—using $\lambda = 0.496$ Å (for $x = 0.0, 0.3, 0.8$). The ambient-pressure XRPD data could be satisfactorily fitted using a tetragonal $P4/mbm$ space group across the whole compositional range, in agreement with previous investigations [4,9].

The XRPD patterns collected under applied pressure at the Xpress beamline reveal that all the investigated samples
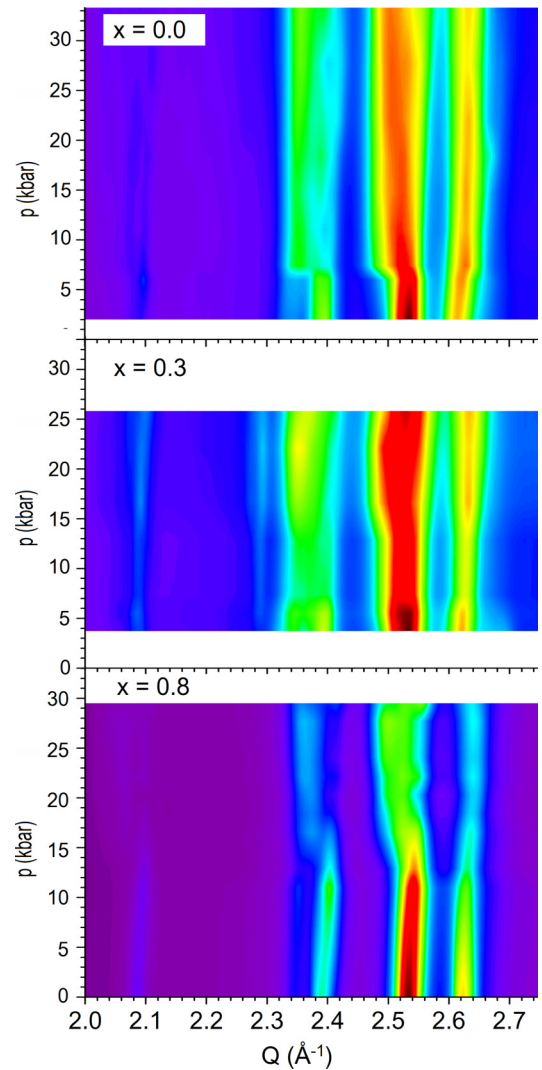

FIG. 7. XRPD patterns as a function of pressure for the $x = 0$, 0.3, and 0.8 samples. Here we show an enlarged view of the Q region where the highest intensity peaks are located and their evolution with the applied pressure.

undergo a structural transition as the pressure increases (Fig. 7). Yb$_2$Pd$_2$In ($x = 0$) exhibits a sharp structural transition at ∼6.5 kbar. In the $x = 0.3$ case, the structural transition has its onset at about the same pressure, but develops over a wider pressure range, to complete at ∼15.0 kbar, thus indicating the first-order character of the transition. For $x = 0.8$, the structural transition is triggered at a significantly higher pressure (∼16 kbar). By inspecting the above data one can deduce that, to some extent, the Sn substitution hinders the formation of the high pressure (HP) phase.

Attempts to ascertain the crystal structure of the HP phase were carried out, notwithstanding the unavoidable background due to the experimental set-up. To this purpose, the HP-XRPD data of the $x = 0$ case were carefully analyzed, since it not only exhibits a complete structural transformation at lower pressures but also because of the lack of a diffraction line broadening due to In substitution. Figure 8 shows the evolution with pressure of the peak located at $Q \sim 2.09$ Å^{-1},

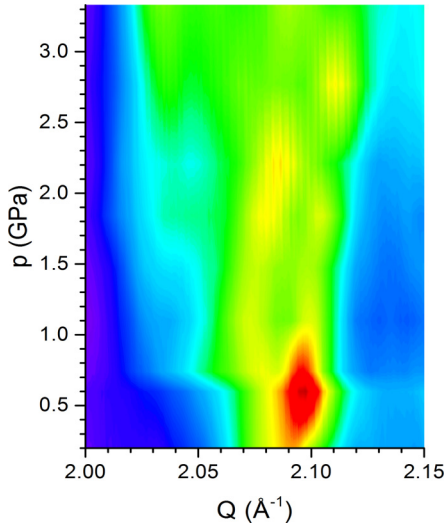FIG. 8. XRPD data showing the evolution with pressure of the diffraction peak located at Q 2.09Å^{-1} for the $x = 0$ case. The 111 reflection pertaining to the low-pressure polymorph splits at a higher pressure, p_{cr}, which marks the structural transition.
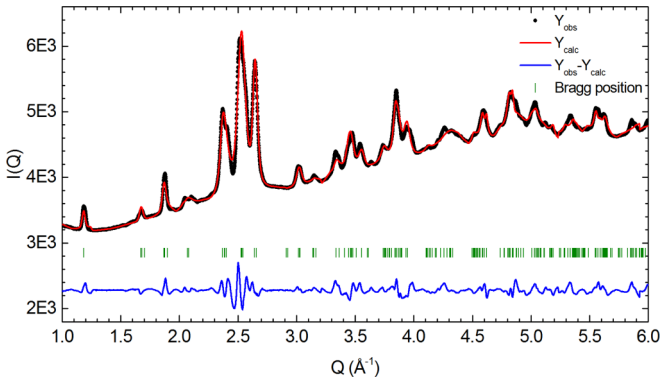

FIG. 9. Rietveld refinement plot for Yb$_2$Pd$_2$In using XRPD data collected at 33.3 kbar and the monoclinic $P2_1/c$ space group.
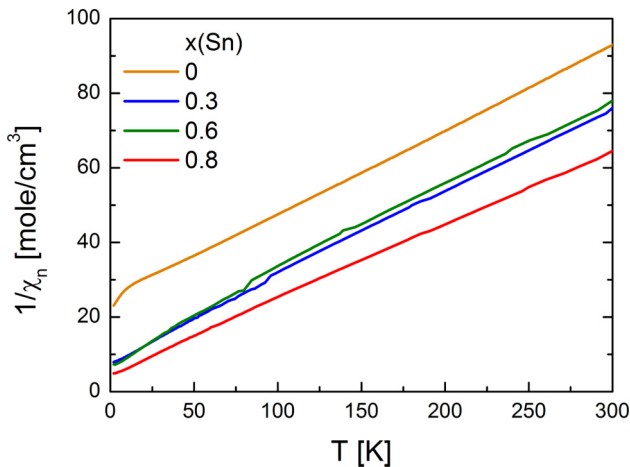

FIG. 10. Temperature-dependent inverse molar susceptibility for the investigated samples. The almost straight lines indicate a Curie-Weiss-like behavior (see text).
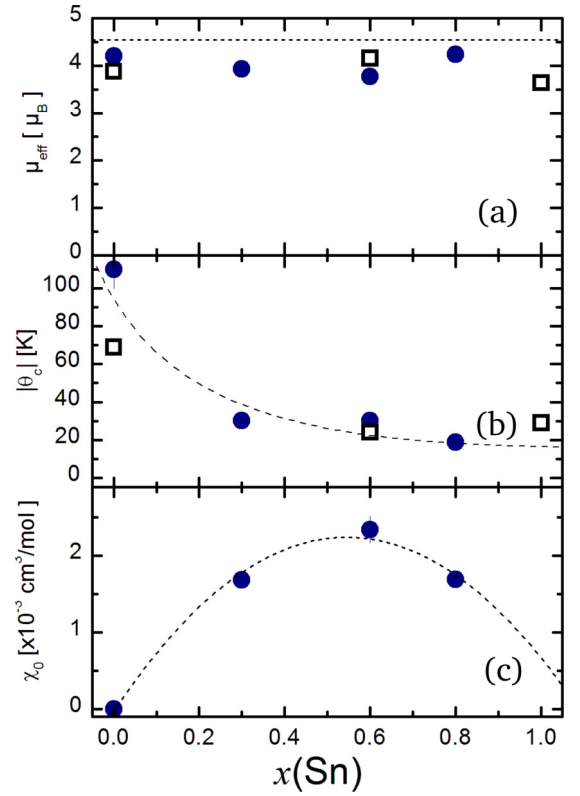

FIG. 11. Fit parameters, as extracted from Curie-Weiss fits of the dc magnetic susceptibility data, vs. Sn content x. Top panel: Effective Yb magnetic moment. The dashed line represents the expected magnetic moment per Yb^{3+} ion. Middle panel: Curie-Weiss temperature. The dashed line is a guide for the eyes. Bottom panel: T-independent contribution χ_0 and parabolic fit. In the first two cases, blue filled circles refer to data from this study; black empty squares are data from Ref. [4].

representing the 111 reflection of the low pressure (LP) phase that splits in the HP polymorph. Such behavior provides some clues and allows us to exclude some of the possible structural models. Firstly, the peak splitting indicates the suppression of the fourfold rotational symmetry. Among the maximal subgroups of the $P4/mbm$ space group, only the orthorhombic space groups $Cmmm$ and $Pbam$ do not contain a fourfold rotational axis. Nevertheless, none of them can account for the observed splitting. On further inspection of the structural models pertaining to the $Cmmm$ and $Pbam$ subgroups, it turns

TABLE II. Yb$_2$Pd$_2$In structural parameters, as refined from XRPD data collected at 290 K and 33.3 kbar (space group $P2_1/c$).

a (Å)	b (Å)	c (Å)	β (deg.)
3.6874(1)	7.5276(1)	7.4740(1)	89.65(1)
Atom	Wyckoff site	x	y	z
Yb	4e	0.5334(3)	0.6679(1)	0.8210(1)
Pd	4e	0.0975(2)	0.1334(1)	0.3787(1)
In	2a	0	0	0

$R_{Bragg} = 2.40, \quad R_{factor} = 1.59$
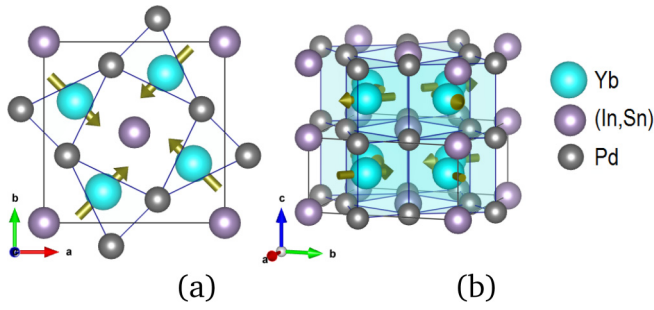
FIG. 12. Magnetic structure of $Yb_2Pd_2In_{1-x}Sn_x$ at ambient pressure, as derived from neutron scattering data [9]. Note the anticollinear in-plane order (a) and the antiferromagnetic intra-layer arrangement (b) of the magnetic Yb^{3+} ($4f^{13}$) ions.

out that the HP phase must be at least monoclinic to reproduce such peak splitting. Several monoclinic models were tested and the best fit of the experimental data was obtained with a $P2_1/c$ structural model. The corresponding Rietveld refinement plot and structural data are reported in Fig. 9 and Table II, respectively. Noteworthy, the R values listed in Table II are somewhat biased toward relatively low values due to the strong instrumental contribution to the diffraction pattern. Therefore, the proposed structural model could differ significantly from the real structure.

APPENDIX B: DC MAGNETIZATION

To assess the bulk magnetic properties of the as-grown samples, systematic dc susceptibility measurements were performed by means of an MPMS and a VSM Dynacool magnetometer systems, both from Quantum Design. $1/\chi(T)$ curves measured from 2 to 300 K at $\mu_0 H = 3$ T are reported in Fig. 10. Data exhibit a clear linear behavior down to about 30–50 K, below which they show a downward curvature. Most likely, this reflects the increasingly stronger correlations between Yb magnetic moments as one approaches the AF ordering temperature. After excluding the low-T data, the magnetic susceptibility between 50 and 300 K could be fitted

by means of a modified Curie Weiss law:

$$\chi_{mol}(T) = \frac{C}{T - \theta} + \chi_0. \qquad (B1)$$

Here C is the Curie constant, θ is the Curie-Weiss temperature, and χ_0 is a constant that accounts for the different temperature-independent contributions. In our case, χ_0 is dominated by the Pauli paramagnetism of the conduction electrons.

Figure 11 summarizes the fit parameters as a function of Sn content x and highlights some interesting features. First, the effective magnetic moment is close to 4.53 μ_B, the expected value for $4f^{13}$ ($^2F_{7/2}$-term) magnetic Yb^{3+} ions, and is mostly independent of the In-Sn substitution rate. Second, the Curie temperature is always negative, thus suggesting a predominance of *antiferromagnetic-like interactions* between Yb^{3+} ions. Finally, the T-independent term χ_0 shows a parabolic dependence vs. Sn content. In particular, it exhibits magnitudes in the 10^{-3} cm³/mol range, with the maximum being reached at optimum doping. We recall that for simple metals χ_0 is about 10^{-6} cm³/mol [35], yet it may increase by more than a factor of 1000 in HF compounds [36]. This is also our case, where the Yb $4f$ electrons hybridize with the conduction electrons, producing a strong enhancement of the carriers' effective mass (HF state).

APPENDIX C: NEUTRON POWDER DIFFRACTION

The magnetic structure of $Yb_2Pd_2In_{1-x}Sn_x$ at ambient pressure, as resulting from neutron diffraction data [9] on an optimally doped compound, is shown in Fig. 12. The anticollinear in-plane ordering of the Yb^{3+} ions, as well as their antiferromagnetic intralayer interactions are in agreement with the magnetometry results.

Because μSR measurements reveal that in all the cases (and in particular for $x = 0.6$) the magnetic phase is greatly enhanced by external pressure, we selected the $x = 0.6$ sample for further neutron powder diffraction (NPD) analysis under applied pressure. To this aim, NPD measurements were performed at the D20 diffractometer of the Institute Laue-Langevin (Grenoble, France) [37]. A TiZr clamp cell
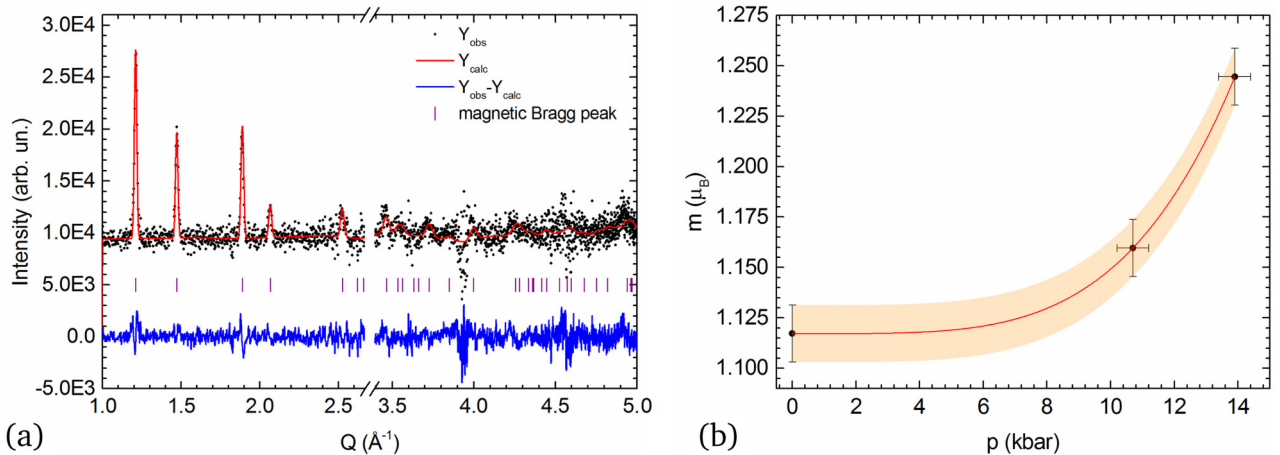

FIG. 13. (a) Coherent magnetic scattering in an $x = 0.6$ sample, measured at 13.9 kbar and 1.5 K, and its Rietveld refinement (see text for details). (b) Evolution with pressure of the of Yb^{3+} magnetic moment as derived from Rietveld fits.

was loaded with about 4 g of sample, using Fluorinert as a pressure transmitting medium. Data were collected at 300 K, as well as in the 1.5 to 5.0 K range (above and below the magnetic transition) using an orange cryostat ($\lambda = 2.4174$ Å). To determine the pressure, a small amount of Pb was added to the sample. The applied pressure was thus directly calculated by substituting the measured structural parameters of Pb into its equation of state.

First, it is worth noting that the low-resolution set-up used to collect the NPD data prevented us from detecting the structural transformation taking place at high pressure. The Rietveld refinement was carried out by fitting the difference between the NPD data collected at 10 K (in the paramagnetic state) and at 1.5 K (in the magnetically ordered state), as shown in Fig. 13(a). No clear evidence of a magnetic phase transition with increasing pressure was observed to $\simeq 14$ kbar, a value where the magnetic structure adopted at ambient pressure [9] is still retained. Nonetheless, we still could detect a moderate increase of the ordered magnetic moment with pressure, as derived by the Rietveld fits shown in Fig. 13(b).

APPENDIX D: DETAILS OF THE DFT CALCULATIONS

To determine the muon site(s) in $Yb_2Pd_2In_{1-x}Sn_x$, we adopted the following strategy: First, we calculated the electrostatic potential in the unit cell. The resulting minima were then used as starting trial positions for the muon, treated in this second step as an impurity in a supercell where all atomic positions are allowed to relax.

The electrostatic potential was calculated using the nonmagnetic Yb_2Pd_2Sn unit cell, which belongs to the $P4/mbm$ space group, with lattice parameters $a = b = 7.5789$ Å and $c = 3.6350$ Å. Here Yb ions occupy the $4h$ Wyckoff positions at (0.1724, 0.6724, 0.5), Pd the $4g$ positions at (0.3716, 0.8716, 0.0), and Sn the $2a$ positions at (0.0, 0.0, 0.0). The potential minima are shown in the isosurface plot of Fig. 14(a). In a second step, the muon was introduced as a hydrogen impurity at the potential minimum, corresponding to the interstitial position (0.45, 0.45, 0.54).

A nonmagnetic $2 \times 2 \times 4$ supercell containing 160 atoms was used to model both Yb_2Pd_2Sn and $Yb_2Pd_2In_{1-x}Sn_x$. Random distributions of In/Sn atoms [$x = 0.5$] were used to account for the substitution. The plane-wave- and pseudopotential-based implementation provided by the Quantum Espresso suite of codes [38] was used for the structural relaxation. For the exchange correlation functional, the
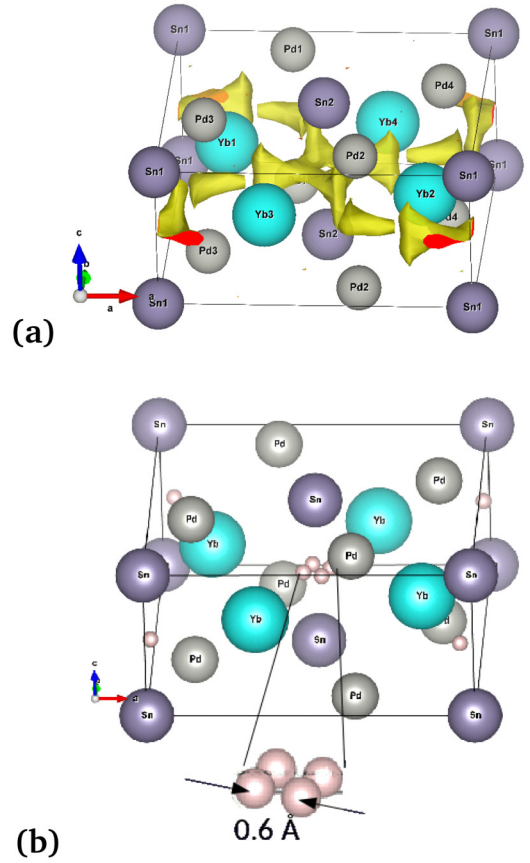

(a)

(b)

0.6 Å

FIG. 14. Muon-stopping sites as obtained from the minima of the electrostatic potential (a) and from self-consistent DFT calculations (b). In the latter case the perturbation caused by muons to the lattice is also accounted for.

Perdew-Burke-Ernzerhof [39] parametrization was used. The core wave function was approximated with the projector augmented wave method for Yb and Pd atoms [40,41] and by the ultrasoft pseudopotential formalism [42,43] for In, Sn, and H. The kinetic and charge density cutoffs were set to 75 and 750 Ry, respectively [44]. The Brillouin zone integration was performed at the gamma point. The force and the total energy were minimized by using 10^{-3} Ry/a.u. and 10^{-4} Ry as thresholds, respectively. The candidate muon site, as resulting from DFT calculations, is shown in Fig. 14(b). This corresponds to four symmetry-equivalent muon-stopping positions, lying only 0.6 Å apart.

TABLE III. The four magnetic structures calculated by using the MAXMAGN code for the parent space group $P2_1/c$, labeled I to IV, that allow nonzero magnetic moments on Yb with a propagation vector (0.5,0, 0.0). Magnetic structure on the four symmetry-equivalent magnetic Yb ions in half of the unit cell, doubled along the x axis.

Label	Mag. group	Yb1	Yb2	Yb3	Yb4
		Magnetic structure[a]			
I	P_a2_1/c	(m_x, m_y, m_z)	(m_x, m_y, m_z)	$(-m_x, m_y, -m_z)$	$(-m_x, m_y, -m_z)$
II	P_a2_1/c	(m_x, m_y, m_z)	$(-m_x, -m_y, -m_z)$	$(-m_x, m_y, -m_z)$	$(m_x, -m_y, m_z)$
III	P_a2_1/c	(m_x, m_y, m_z)	(m_x, m_y, m_z)	$(m_x, -m_y, m_z)$	$(m_x, -m_y, m_z)$
IV	P_a2_1/c	(m_x, m_y, m_z)	$(-m_x, -m_y, -m_z)$	$(m_x, -m_y, m_z)$	$(-m_x, m_y, -m_z)$

[a]Yb1, Yb2, Yb3, Yb4 at (0.2667, 0.66790, 0.82100), (0.2333, 0.33210, 0.17900), (0.2333, 0.1679, 0.6790), and (0.2667, 0.8321, 0.32100).

TABLE IV. Calculated muon dipolar field B_{dip} in units of mT.[a]

Label	$m_x = 0, m_y = m_z$	$m_x = 0, -m_y = m_z$	$m_x = 1, m_y = m_z = 0$	$m_y = 1, m_x = m_z = 0$	$m_z = 1, m_x = m_y = 0$
			B_{dip} (mT)		
I	234.03	99.74	25.93	117.09	225.85
II	0.0	0.0	0.0	0.0	0.0
III	234.19	103.55	251.90	216.13	137.32
IV	0.0	0.0	0.0	0.0	0.0

[a]Dipolar field at the muon position (0.5, 0.5, 0.5). The substitution-induced distortions on the Yb ions were considered for the Sn/In ($x = 0.5$) case.

We also verified that the transition to a monoclinic structure (occurring at high pressure) does not modify the local magnetic field at the muon site. For this, we selected the four irreducible representations allowed by the monoclinic HP structure (space group $P2\bar{1}/c$) with nonzero magnetic moment on the Yb ion, as detailed in Table III. Then we calculated the dipolar field at the muon implantation sites in all these configurations, as shown in Table IV. It is worth noting that B_μ is almost unchanged for all the structures except III, where $B_{dip} = 25.92$ mT.

APPENDIX E: AVERAGING THE DIPOLAR FIELDS AND ACCOUNTING FOR THE EFFECTS OF STRUCTURAL DISTORTION

The averaging over four equivalent off-center sites leads to small deviations from the field value calculated at (0.5,0.5,0.5). For completeness, in Table V, we summarize the results obtained using both approaches. Only three configurations (here shown in bold) exhibit substantial magnetic fields at the muon stopping site.

TABLE V. Calculated dipolar field values B_{dip} at the (0.5,0.5,0.5) muon-stopping site, compared to those obtained after averaging over four symmetry-equivalent muon positions, $\langle B_{dip} \rangle$. The 10 maximal magnetic space groups of the parent $P4/mbm$ space group are here labeled I to X. Dipolar fields for the Yb ions at the undistorted symmetry positions (undist.) and those displaced from symmetry position induced by Sn/In substitution (dist.).

Label	B_{dip} (mT)		$\langle B_{dip} \rangle$ (mT)	
	Undist.	Dist.	Undist.	Dist.
I	0.0	6.18 (1.91)	0.0	6.37 (1.97)
II	0.0	3.79 (1.66)	0.0	3.86 (1.69)
III	0.0	3.58 (1.76)	0.0	3.71 (1.87)
IV	242.16	245.22 (4.96)	248.65	251.83 (5.20)
V	0.0	4.66 (1.68)	0.0	4.74 (1.71)
VI	0.0	6.87 (1.89)	0.0	7.06 (1.95)
VII	0.0	2.25 (1.21)	0.0	2.36 (1.27)
VIII	121.08	122.61 (4.53)	124.32	125.91 (4.68)
IX	0.0	3.03 (1.25)	0.0	3.19 (1.29)
X	96.99	100.17 (4.54)	99.26	102.50 (4.64)

[1] P. Gegenwart, J. Custers, C. Geibel, K. Neumaier, T. Tayama, K. Tenya, O. Trovarelli, and F. Steglich, Magnetic-Field Induced Quantum Critical Point in YbRh$_2$Si$_2$, Phys. Rev. Lett. **89**, 056402 (2002).

[2] P. Gegenwart, Q. Si, and F. Steglich, Quantum criticality in heavy-fermion metals, Nat. Phys. **4**, 186 (2008).

[3] E. Bauer, G. Hilscher, H. Michor, C. Paul, Y. Aoki, H. Sato, M. Giovannini, and A. Saccone, Evolution of ground state properties in novel Yb$_2$Pd$_2$In$_{1-x}$Sn$_x$, J. Magn. Magn. Mater. **272–276**, 237 (2004).

[4] E. Bauer, G. Hilscher, H. Michor, C. Paul, Y. Aoki, H. Sato, D. T. Adroja, J.-G. Park, P. Bonville, C. Godart, J. Sereni, M. Giovannini, and A. Saccone, The magnetic instability of Yb$_2$Pd$_2$(In, Sn) in a non-Fermi liquid environment, J. Phys.: Condens. Matter **17**, S999 (2005).

[5] E. Bauer, R. T. Khan, M. Giovannini, and C. Ritter, Appearance of long range magnetic order in a nonmagnetic periphery: Yb$_2$Pd$_2$(In, Sn), Phys. Status Solidi B **247**, 717 (2010).

[6] T. Muramatsu, T. Kanemasa, T. Kagayama, K. Shimizu, Y. Aoki, H. Sato, M. Giovannini, P. Bonville, V. Zlatic, I. Aviani, R. Khasanov, C. Rusu, A. Amato, K. Mydeen, M. Nicklas, H. Michor, and E. Bauer, Reentrant quantum criticality in Yb$_2$Pd$_2$Sn, Phys. Rev. B **83**, 180404(R) (2011).

[7] H. Yamaoka, N. Tsujii, M.-T. Suzuki, Y. Yamamoto, I. Jarrige, H. Sato, J.-F. Lin, T. Mito, J. Mizuki, H. Sakurai, O. Sakai, N. Hiraoka, H. Ishii, K.-D. Tsuei, M. Giovannini, and E. Bauer, Pressure-induced anomalous valence crossover in cubic YbCu$_5$-based compounds, Sci. Rep. **7**, 5846 (2017).

[8] In some cases we observed only tiny fractions of YbPd$_2$In.

[9] A. Martinelli, S. Sanna, G. Lamura, C. Ritter, B. Joseph, E. Bauer, and M. Giovannini, Structural and magnetic properties of the Yb$_2$Pd$_2$In$_{1-x}$Sn$_x$ system: A synchrotron x-ray and neutron powder diffraction investigation, J. Phys.: Condens. Matter **31**, 385802 (2019).

[10] R. Khasanov, Z. Guguchia, A. Maisuradze, D. Andreica, M. Elender, A. Raselli, Z. Shermadini, T. Goko, F. Knecht, E. Morenzoni, and A. Amato, High pressure research using muons at the Paul Scherrer Institute, High Press. Res. **36**, 140 (2016).

[11] Z. Shermadini, R. Khasanov, M. Elender, G. Simutis, Z. Guguchia, K. V. Kamenev, and A. Amato, A low-background piston-cylinder-type hybrid high pressure cell for muon-spin rotation/relaxation experiments, High Press. Res. **37**, 449 (2017).

[12] The background contribution from the Ag sample holder (plate no. 233) was determined via transverse-field experiments at $\mu_0 H = 3$ mT and 20 mK: $a_{bg} \sim 0.25$ and $\lambda_{bg} = 0.0158(9)\mu s^{-1}$.

[13] A transverse-field μSR experiment at high temperature ($T >$ T_N) was used to determine a_{bg} ($\sim$65%). This parameter was then kept fixed during the subsequent fit iterations.

[14] The K-T Gaussian depolarization rate σ_{bg}^G (static dipolar nuclear contribution) and λ_{bg} (dynamic electronic contribution) were determined by fitting the ZF-asymmetry at long times, where the depolarization rate is dominated by the pressure cell. Both parameters were then kept fixed during the subsequent fit iterations except λ_{bg} for $T < 1$ K.

[15] We note that the choice of a zero order Bessel function for the oscillating component does not improve the fit in all the tested samples.

[16] T. Shiroka, G. Lamura, S. Sanna, G. Prando, R. De Renzi, M. Tropeano, M. R. Cimberle, A. Martinelli, C. Bernini, A. Palenzona, R. Fittipaldi, A. Vecchione, P. Carretta, A. S. Siri, C. Ferdeghini, and M. Putti, Long- to short-range magnetic order in fluorine-doped CeFeAsO, Phys. Rev. B **84**, 195123 (2011).

[17] In magnetically ordered polycrystalline samples with isotropically distributed domains, statistically 1/3 of the implanted muons probe a local field parallel to their initial polarization, whereas 2/3 of them sense a local field orthogonal to their initial polarization.

[18] O. Isnard, C. Rusu, R. Dudric, D. Andreica, A. Amato, and B. Chevalier, Low-temperature and high-pressure μSR study of the strongly correlated CeNiSnH$_x$ compounds, Phys. Rev. B **93**, 224424 (2016).

[19] J. S. Möller, P. Bonfà, D. Ceresoli, F. Bernardini, S. J. Blundell, T. Lancaster, R. De Renzi, N. Marzari, I. Watanabe, S. Sulaiman, and M. I. Mohamed-Ibrahim, Playing quantum hide-and-seek with the muon: Localizing muon stopping sites, Phys. Scr. **88**, 068510 (2013).

[20] F. Bernardini, P. Bonfà, S. Massidda, and R. De Renzi, Ab initio strategy for muon site assignment in wide band gap fluorides, Phys. Rev. B **87**, 115148 (2013).

[21] P. Bonfà, F. Sartori, and R. De Renzi, Efficient and reliable strategy for identifying muon sites based on the double adiabatic approximation, J. Phys. Chem. C **119**, 4278 (2015).

[22] P. Bonfà and R. De Renzi, Toward the computational prediction of muon sites and interaction parameters, J. Phys. Soc. Jpn. **85**, 091014 (2016).

[23] S. C. Cheung, Z. Guguchia, B. A. Frandsen, Z. Gong, K. Yamakawa, D. E. Almeida, I. J. Onuorah, P. Bonfà, E. Miranda, W. Wang, D. W. Tam, Y. Song, C. Cao, Y. Cai, A. M. Hallas, M. N. Wilson, T. J. S. Munsie, G. Luke, B. Chen, G. Dai, C. Jin, S. Guo, F. Ning, R. M. Fernandes, R. De Renzi, P. Dai, and Y. J. Uemura, Disentangling superconducting and magnetic orders in NaFe$_{1-x}$Ni$_x$As using muon spin rotation, Phys. Rev. B **97**, 224508 (2018).

[24] B. H. Bernhard, B. Coqblin, and C. Lacroix, Frustration in the Kondo lattice model: Local versus extended singlet phases, Phys. Rev. B **83**, 214427 (2011).

[25] Bilbao Crystallogr. Server, Maxmagn: Maximal magnetic space groups for a given propagation vector and resulting magnetic structural models: https://www.cryst.ehu.es/cgi-bin/cryst/programs/msglist2.pl. See also Ref. [26] for further details.

[26] J. M. Perez-Mato, S. V. Gallego, E. S. Tasci, L. Elcoro, G. de la Flor, and M. I. Aroyo, Symmetry-based computational tools for magnetic crystallography, Annu. Rev. Mater. Res. **45**, 217 (2015).

[27] K. Momma and F. Izumi, *VESTA*: A three-dimensional visualization system for electronic and structural analysis, J. Appl. Crystallogr. **41**, 653 (2008).

[28] S. Doniach, The Kondo lattice and weak antiferromagnetism, Physica B+C **91**, 231 (1977).

[29] E. Bauer, S. Berger, S. Gabani, G. Hilscher, H. Michor, C. Paul, M. Giovannini, A. Saccone, C. Godart, P. Bonville, Y. Aoki, and H. Sato, Non-Fermi-liquid features of novel Yb$_2$Pd$_2$In, Acta Phys. Pol. B **34**, 367 (2003).

[30] M. Giovannini (private communications, 2018).

[31] J. Flouquet and H. Harima, Heavy fermion material: Ce versus Yb case, Kotai Butsuri **2**, 47 (2012); arXiv:0910.3110.

[32] D. Braithwaite, A. Fernandez-Pañella, E. Colombier, B. Salce, G. Knebel, G. Lapertot, V. Balédent, J.-P. Rueff, L. Paolasini, R. Verbeni, and J. Flouquet, (p, T, H) phase diagram of heavy fermion systems: Some systematics and some surprises from ytterbium, J. Supercond. Novel Magn. **26**, 1775 (2013).

[33] A. Fernandez-Pañella, D. Braithwaite, B. Salce, G. Lapertot, and J. Flouquet, Ferromagnetism in YbCu$_2$Si$_2$ at high pressure, Phys. Rev. B **84**, 134416 (2011).

[34] G. Knebel, R. Boursier, E. Hassinger, G. Lapertot, P. G. Niklowitz, A. Pourret, B. Salce, J. P. Sanchez, I. Sheikin, P. Bonville, H. Harima, and J. Flouquet, Localization of 4f state in YbRh$_2$Si$_2$ under magnetic field and high pressure: Comparison with CeRh$_2$Si$_2$, J. Phys. Soc. Jpn. **75**, 114709 (2006).

[35] N. W. Ashcroft and N. D. Mermin, *Solid State Physics* (Saunders College Publishing, Philadelphia, 1976).

[36] P. Gegenwart, J. Custers, Y. Tokiwa, C. Geibel, and F. Steglich, Ferromagnetic Quantum Critical Fluctuations in YbRh$_2$(Si$_{0.95}$Ge$_{0.05}$)$_2$, Phys. Rev. Lett. **94**, 076402 (2005).

[37] G. Lamura, A. Martinelli, and C. Ritter, The magnetic structure of Yb$_2$Pd$_2$(In$_{1-x}$Sn$_x$) as a function of applied pressure (2018), doi:10.5291/ILL-DATA.5-31-2584.

[38] P. Giannozzi, O. Andreussi, T. Brumme, O. Bunau, M. Buongiorno Nardelli, M. Calandra, R. Car, C. Cavazzoni, D. Ceresoli, N. Cococcioni, N. Colonna, I. Carnimeo, A. Dal Corso, S. de Gironcoli, P. Delugas, R. A. DiStasio Jr., A. Ferretti, A. Floris, G. Fratesi, G. Fugallo, R. Gebauer, U. Gerstmann, F. Giustino, T. Gorni, J. Jia, M. Kawamura, H.-Y. Ko, A. Kokalj, E. Küçükbenli, M. Lazzeri, M. Marsili, N. Marzari, F. Mauri, N. L. Nguyen, H.-V. Nguyen, A. Otero-de-la-Roza, L. Paulatto, S. Poncé, D. Rocca, R. Sabatini, B. Santra, M. Schlipf, A. P. Seitsonen, A. Smogunov, I. Timrov, T. Thonhauser, P. Umari, N. Vast, X. Wu, and S. Baroni, Advanced capabilities for materials modelling with Quantum ESPRESSO, J. Phys.: Condens. Matter **29**, 465901 (2017) and references therein.

[39] J. P. Perdew, K. Burke, and M. Ernzerhof, Generalized Gradient Approximation Made Simple, Phys. Rev. Lett. **77**, 3865 (1996).

[40] P. E. Blöchl, Projector augmented-wave method, Phys. Rev. B **50**, 17953 (1994).

[41] A. Dal Corso, Pseudopotentials periodic table: From H to Pu, Comput. Mater. Sci. **95**, 337 (2014).

[42] D. Vanderbilt, Soft self-consistent pseudopotentials in a generalized eigenvalue formalism, Phys. Rev. B **41**, 7892 (1990).

[43] K. F. Garrity, J. W. Bennett, K. M. Rabe, and D. Vanderbilt, Pseudopotentials for high-throughput DFT calculations, Comput. Mater. Sci. **81**, 446 (2014).

[44] These values compare well with the convergence tests available at https://www.materialscloud.org/discover/sssp/table/efficiency and described in Refs. [45,46].

[45] E. Küçükbenli, M. Monni, B. I. Adetunji, X. Ge, G. A. Adebayo, N. Marzari, S. de Gironcoli, and A. Dal Corso, Projector augmented-wave and all-electron calculations across the periodic table: A comparison of structural and energetic properties, arXiv:1404.3015.

[46] K. Lejaeghere *et al.*, Reproducibility in density functional theory calculations of solids, Science **351**, aad3000 (2016).